Volume xx (200y), Number z, pp. 1–13

Visual Ensemble Analysis with Deep Learning Prediction for Studying the Effect of Tissue Properties on Radiofrequency Ablation

R. Sabbagh Gol[1], M. Evers[1,2], K. Heimes[1], T. Gerrits[1,3], S. Gyawali[4], D. Sinden[5], T. Preusser[4,5], and L. Linsen[1]

[1]University of Münster, Germany [2]University of Stuttgart, Germany [3]RWTH Aachen University, Germany
[4]Constructor University, Bremen, Germany [5]Fraunhofer Institute for Digital Medicine MEVIS, Bremen, Germany

Abstract

Radiofrequency ablation refers to a minimally invasive tumor ablation treatment using radiofrequency electromagnetic waves. A needle is placed inside the tumor, and an electrical current is applied, which is heating the tissue to burn the tumor. For treatment planning, the heat propagation is simulated, but the treatment volumes are significantly affected by the tissue properties, which vary between different patients, based upon both the vasculature and levels of fat and water content. Undertreatment can lead to tumor recurrence, while over-treatment damages healthy tissue. We propose to study the effect of tissue properties on the ablation based on an interactive visual analysis of simulation ensembles, where the tissue properties form the parameter space of the ensemble. The proposed Tissue Property Analysis Tool (TPAT) uses 2D and 3D spatial visualizations for comparative analysis of simulation outcomes for different parameter settings. A 3D parameter-space visualization allows for the analysis of the effect on the ablation result when modifying a selected parameter for the three involved tissues (tumor, liver, and vessels). During the analysis, any parameter setting shall be accessible. When no simulation outcome has been generated for a selected parameter setting, we deploy a deep learning-based surrogate model to predict an ablation outcome. Using our deep learning approach, we achieve an improved prediction accuracy both within and across spatial configurations, which outperforms interpolation-based schemes in 94.32% and 99.07% of the test data, respectively. We discuss our approach with domain experts for developing simulation models and demonstrate the usefulness of our approach for analyzing the effect of tissue properties on radiofrequency ablation of liver tumors.

1. Introduction

Cancer is one of the leading causes of death worldwide, and its successful treatment, therefore, is of utmost importance to our society. Radiofrequency (RF) ablation is a treatment that comes with the advantage of being minimally invasive and is typically applied in lung, liver, kidney, or bones [BFAC18]. A needle is placed inside the malignant tissue, which is then ablated using radiofrequency electromagnetic waves to cause a coagulative necrosis, i.e., the cells are heated until they are destroyed. To ensure that the entire malignant tissue is ablated while keeping as much healthy tissue alive as possible, proper treatment planning for the needle placement is required. Simulation of the heat propagation provides a means to estimate the ablation area [Ber06]. However, for generating a simulation outcome, one needs to set a number of parameters for the properties (such as blood perfusion or thermal conductivity) of the involved tissues. Due to inter-subject variability, the choice of these parameters introduces a substantial amount of uncertainty to the simulation output [SCTL05, ALHG08].

In this paper, we present a visual analysis tool that allows experts to study the effect of tissue properties on the RF ablation outcome, where the variability concerning changing tissue properties is captured by a simulation ensemble, where the tissue properties of the involved tissues form its multi-dimensional parameter space. We present the Tissue Property Analysis Tool (TPAT) that uses interactive visualizations to analyze the simulation ensembles. The spatial domain is visualized using 2D and 3D visualization methods of the simulation output and its anatomical context, as well as of the differences in simulation outputs for a comparative analysis of different parameter settings. Moreover, quantitative measures are computed and can be compared. A 3D parameter-space visualization allows for the analysis of the effect of a selected tissue parameter on the ablation outcome for the three tissues involved. Individual parameter settings can be selected for comparison using a selection widget based on parallel coordinates. For a continuous exploration of the parameter space, any parameter configuration can be chosen, i.e., also those for which no simulation has been computed. As computing new simulation runs is computationally intense, it is not feasible to compute them on the fly within an interactive analysis system. Instead, we propose to train a deep neural network that allows us to predict the simulation outcome. We demonstrate the effectiveness of using TPAT for studying the influence of tissue properties on RF ablation and present feedback from domain experts who work on the development of RF ablation simulations.

We further analyze the prediction quality of our deep learning approach. Our main contributions can be summarized as follows:

- The design of TPAT for an interactive visualization and quantitative evaluation of RF ablation outcomes within simulation ensembles.
- Comparative spatial visualizations of increase and decrease in ablation volumes for different RF ablation simulation runs.
- Interactive 3D parameter-space visualization to provide an overview of the ablation simulation outcome when altering a selected tissue parameter for the three involved tissues.
- A deep learning-based surrogate model to predict simulation outcome for parameter settings, where no simulation outcome exists.
- Application of TPAT to an extensive liver tumor use case.

This paper is an extension of our awarded paper presented at the 12th Eurographics Workshop on Visual Computing in Biology and Medicine (VCBM 2022) [HEG*22]. While our previous work introduced TPAT for interactive ensemble visualization, the current work extends this concept by (1) integrating a deep learning-based surrogate model directly into the visual analysis workflow, enabling continuous exploration of unseen parameter combinations in real time, (2) the analysis of the prediction quality in terms of visualizations and quantitative ablation measures, and (3) a comparison of the prediction outcome to the scattered data interpolation method that was used in the original paper.

2. Related Work

Visualization of medical simulations. Visual analyses of simulations in medical applications help to understand the underlying phenomena. Raidou et al. [RCMM*16] introduce a framework to evaluate radiotherapy data via tumor control probability models that quantify the probability of effective tumor treatment. Ristovski et al. [RGH*19] tackle RF ablation uncertainty and propose an uncertainty-aware visual analysis approach of a stochastic simulation model. Rieder et al. [RWS*10] propose a traffic light coloring scheme within a tumor map to visualize the ablation state of the tumor in 3D space. Bricault et al. [BKM*06] introduce a semi-automated 3D segmentation process to distinguish the remaining part of tissue after ablation treatment. Our goal deviates from the goals of the approaches listed above, as we try to analyze the effect of tissue properties on the ablation simulation outcome.

Ensemble visualization. Approaches to analyze spatio-temporal simulation ensembles often include the analysis of statistical properties [PWB*09, SZD*10] or clustering [PBCR11, HHB16, FKRW17, ME19, KBL19b, KBL19a]. A recent survey discusses different aspects of ensemble visualization [WHLS19]. Comparative visualization of ensemble members was proposed by Phadke et al. [PPA*12], but they do not systematically analyze the parameter space. In this paper, we propose a tool that allows for comparative visualization of individual ensemble members as well as overview visualizations of the parameter space with respect to the simulation outcome.

Parameter-space visualization. Sedlmair et al. [SHB*14] present a conceptual framework for parameter-space analysis, where they identify six analysis tasks. Among those, we address the sensitivity to the input parameters (tissue properties), which also relates to the analysis of parameter-induced uncertainty (uncertainty in tumor ablation). Recently, an approach for investigating the parameter sensitivity and its spatial variations has been proposed [ELRL24]. However, they do not investigate domain-specific measures for RF ablation. For parameter-space analysis, different visual encodings such as radial layouts, glyph-based visualizations, projections, and dimensionality reduction are used [BM10, BPM*15, STDS95, OKB*19]. We apply parallel coordinates to navigate through the parameter space [OBJ15, WLSL17]. For visualizing the effect of a selected tissue property on the ablation outcome, we propose a 3D parameter-space visualization, where the three dimensions are formed by the selected tissue property for the three tissues involved. Evers et al. [EL22] propose visualizing multi-dimensional parameter spaces using a hyper-slicer, but as the RF ablation simulations only involve three tissues, we can restrict ourselves to 3D visualizations. Moreover, we combine parameter-space analysis with domain-specific, comparative spatial visualizations, which is not addressed by any other approach.

Deep learning for visualization. Existing work on parameter space exploration can be categorized into two main approaches: traditional methods without surrogate models and those utilizing surrogate models. Traditional methods focus on analyzing collected simulation input-output pairs which are limited as they cannot explore unsimulated input parameters. Surrogate models, including our deep learning-based surrogate model, address this limitation by predicting simulation outputs for new input parameters, thus enabling more comprehensive parameter space exploration [HWG*19]. On the other hand, deep learning models help the visualization community in different tasks such as generating suitable visualizations [DD19, LQT*18], improving the efficiency of visualization creation [CWB*19], interpreting insights [CZW*19], or imitating layouts and color selection [HL22, WJW*19, SWS19]. A recent survey summarizes the different contributions [WH23]. Most related to our use of deep learning methodology is probably InSituNet [HWG*19] and VDL-Surrogate [SXL*22], where a deep neural network is trained with a simulation ensemble to generate visualizations of unknown simulation runs. Moreover, Zhao et al. provide a comprehensive overview of deep learning approaches in image-guided tumor ablation, emphasizing the increasing importance of data-driven prediction methods in treatment planning [ZHXS25]. Despite advances in ensemble visualization, few systems have seamlessly coupled deep learning surrogates with interactive analysis interfaces to extend exploration beyond precomputed simulations. TPAT bridges this gap and allows for visual and quantitative analysis of the predicted outcome instead of only generating an output image.

3. Tissue Property Analysis Tool (TPAT)

In the following, we will introduce the Tissue Property Analysis Tool (TPAT) describing the analysis tasks, the visual designs for (comparative) spatial and parameter-space visualizations, the quantitative ablation measures, and finally the deep learning prediction of ablation outcomes.

3.1. Task Analysis

TPAT was developed in close collaboration with domain experts in the field of RF ablation simulations. Within several rounds of discussion, the following analysis tasks were identified to be most crucial:

T1: *Visualizing the ablation volume for different tissue properties*: The spatial extent of the ablation volume shall be investigated to observe which tissues are affected by how much. In particular, users should be able to examine the ablated region for a given parameter configuration, assessing tumor coverage (including safety margins) and unintended damage to healthy tissue. Spatial context (such as nearby vessels) shall be included to support accurate interpretation.

T2: *Comparison of ablation volumes*: To understand how tissue parameters influence the ablation, it should be possible for users to compare spatial differences between simulation runs, focusing on changes in ablation shape, size, and local effects near critical structures.

T3: *Identifying the most significant tissue properties*: Given the high number of parameters, users would like to detect, which tissue properties have the strongest impact on the ablation outcome to reduce the effective parameter space.

T4: *Analysis of ablation measures with varying tissue properties*: Quantitative measures (e.g., ablation volume, tumor coverage, healthy-tissue damage, Dice coefficient) shall be derived that allow for a numerical assessment of the ablation volume change when altering tissue properties.

T5: *Continuous parameter-space analysis*: The continuous transition of parameter settings of tissue properties within the parameter space shall be supported, which requires predicting new simulation outcomes at interactive rates.

3.2. System Overview

To address the defined analysis tasks, TPAT, an integrated visual analytics approach, is developed. TPAT combines ensemble simulations with a deep learning surrogate model that predicts outcomes for unsimulated parameter settings. While the visualizations and derived quantitative measures enable comparative analyses of ablation volumes across simulation runs (Tasks T1, T2, T4), parameter-space visualizations facilitate the identification of the most influential tissue properties (Task T3), and the integrated surrogate model enables continuous parameter-space exploration through real-time prediction of new simulation outcomes (Task T5). Both simulated and predicted results are seamlessly visualized within the same interface, allowing experts to study tissue property effects interactively and efficiently.

3.3. Visual Design

The visual design of TPAT consists of multiple coordinated views as shown in Figure 1. We refer to the accompanying video for a demonstration of the interactive use of TPAT.

Spatial visualizations. The 2D and 3D spatial views are the main tools to observe volumetric changes in the ablation area due to different tissue property values (Task T1). The *3D volume visualization* (Figure 1a) visualizes the ablated volume by creating an isosurface for temperature value 54 °C of the output temperature field of the simulation. Alternatives like glyph-based visualizations were considered, but surface-based visualizations show the most relevant structures within their 3D spatial constellation for a quick understanding of ablation volume extent and surrounding influencing factors. It is also possible to show a *safety margin* around the tumor, which is commonly added for treatment planning. In our tool, the size of the margin can be defined by the user. To provide context, the labeled tissues (here tumor, liver, and blood vessels) are displayed. In addition, a *slice viewer* (Figure 1b) presents the same data as the 3D visualization but shows only a single interactively adjustable slice, thus avoiding occlusion. It also enables users to measure distances directly within the slice by right-clicking and dragging, which helps to quantify volumetric changes of the ablation region. We chose a slice-based visualization to complement the 3D rendering for detailed local comparison (Task T2), as slices avoid occlusion, allow for precise distance measurements, and are commonly used in the medical domain, thus, familiar to experts.

To enable a *comparative visualization* of two volumes (Task T2), we compute the ablation intersection volumes by comparing the ablation volume of the current tissue property values with the ablation volume of a reference setting. We compute the differences of the calculated ablation volumes and refer to them as *expansion* and *reduction volume*, which indicate in which spatial regions the current ablation volume is larger or smaller than the reference (see Figure 2). The multi-dimensional tissue property values of the current and the reference setting can be selected using *parallel coordinates* (Figure 1d). Parallel coordinates are chosen as they scale well with dimensionality and allow for an intuitive and precise selection of values on individual axes (required for all tasks). Scatterplot matrices (SPLOMs) were considered as an alternative, but were rejected, as they need more space. All spatial visualizations can be applied to both simulation results and ablation volumes predicted by the surrogate model.

Parameter-space visualizations. For detecting the most influential tissue properties (Task T3) and investigating changes in ablation measures when varying tissue properties (Task T4), we deploy parameter-space visualizations. We use a 3D layout for these visualizations, where the three Cartesian coordinate axes represent the values of an interactively selected tissue property for each of the three tissue types. RF ablation simulations typically model healthy tissue (e.g. liver), malignant tissue (e.g. tumor), and blood vessels. In the *dataset distribution plot* (Figure 3), a 3D scatterplot (grey spheres) of the parameter-space sampling is shown. Alternatives such as dimensionality reduction (PCA, UMAP) were discussed but rejected because they obscure the direct interpretation of the three parameter axes, which domain experts required. A SPLOM would also be an alternative but might lead to overplotting because of the projection along one dimension. The user can interactively select a simulation run by clicking on a sphere, which is then highlighted in green (and its k nearest neighbors in blue). All other views are updated accordingly.

The *ablation data plot* (Figure 1e) uses the same 3D Cartesian coordinates as the dataset distribution plot and is a novel visualization method to investigate the influence of tissue properties on the ablation outcome. Alternatives would have been 2D heatmaps or

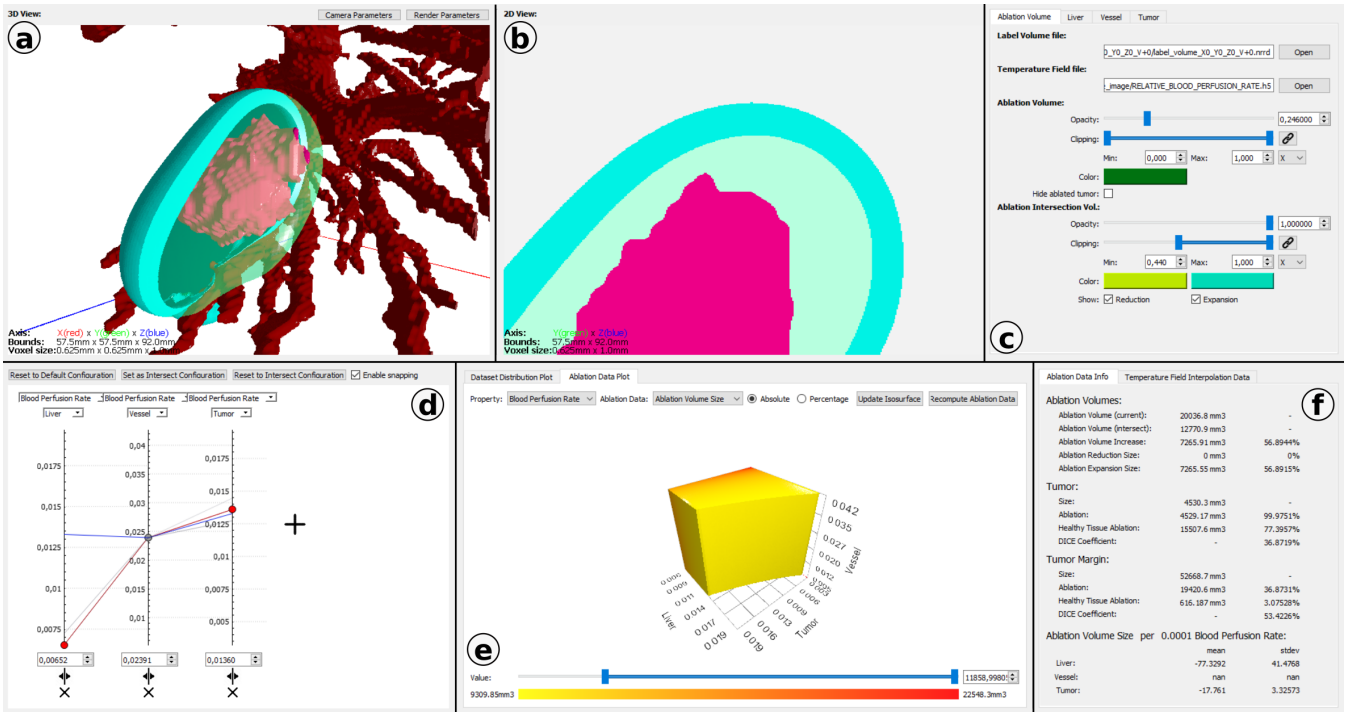

Figure 1: The Tissue Property Analysis Tool (TPAT) contains a user interface with 6 linked views. A 3D visualization (a) and a 2D visualization (b) provide spatial information whose representation can be adjusted interactively (c). Here, the tumor is shown in pink, the ablation zone in light green, the safety margin in light blue, and the vessels in dark red. The user can select parameter settings in the parallel coordinates (d) which are used for selecting the data for the spatial and comparative visualizations. The parameter space is visualized in the ablation data plot (e), while quantitative information about the ablation measures is also shown numerically (f).

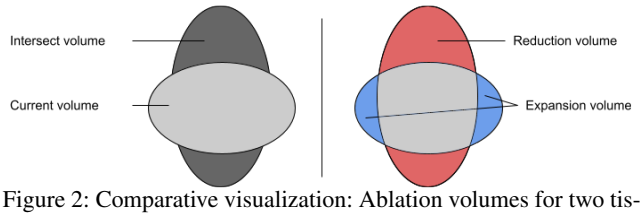

Figure 2: Comparative visualization: Ablation volumes for two tissue properties are compared by calculating expansion (blue) and reduction (red) volumes, illustrated schematically in 2D.

projected scatterplots with color-coding, but they either reduced the dimensional structure or made it harder for users to relate specific parameter combinations to the ablation outcome. The user selects an ablation measure (cf. Section 3.4) that shall be applied to judge the impact of tissue properties on the ablation outcome. Then, the user defines an interval of the selected metric's range with a slider that is located below the plot (see Figure 1e). The plot then shows a surface in the 3D parameter subspace which surrounds all parameter settings, where the ablation measure's values lie in the chosen value range. The surface is given in the form of two isosurfaces, one for the lower and one for the upper limit of the selected interval, which are connected along the boundary of the 3D parameter subspace to enclose all points, where the ablation measure's values are between that lower and upper limit. In addition, the surface is color-coded with respect to the ablation measure's values. The color gradient provides a hint about the influence of the selected tissue property (Task T3). The interactive exploration of the parameter space using the surfaces allows the user to easily inspect where the ablation measure values are particularly high or low for the specific tissue property. Moreover, it can be used to investigate certain points of interest in the parameter space where the ablation measure suddenly responds differently to property value changes (Task T4). The 3D visualization also supports a direct comparison of the different tissues, as one can see how the isosurface varies if the selected range is changed. The interactive exploration also exhibits the presence of non-linearities by variations in the speed of change of the surface.

3.4. Quantitative Measures

For the interactive analysis of the tissue properties' influence on the ablation outcome (Task T4), multiple measures are supported that quantify volumes and differences between volumes. The computed measures for the selected simulation run are displayed in a sidebar (Figure 1f) and can be selected for the visualization within the ablation data plot (cf. Section 3.3). Supported measures are, among others, sizes of *ablation volume*, *tumor ablation volume*, and *healthy tissue ablation volume* [HEG*22], all with or without a safety margin. In the case studies in Section 4, we will mainly make use of the sizes of the *ablation volume* (in mm^3) and of the *tumor ablation volume* (in mm^3 or %), i.e., how much of the tumor gets ablated.

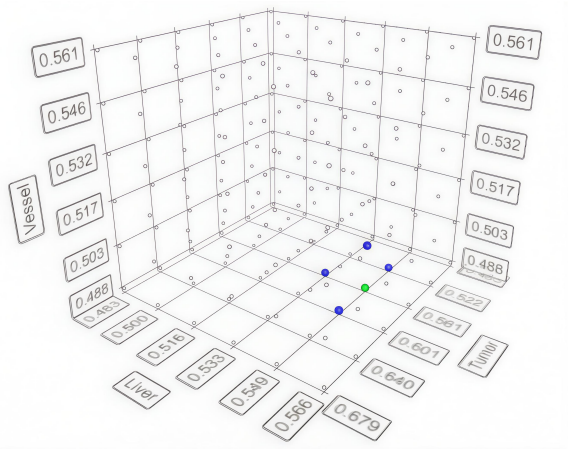

Figure 3: Dataset distribution plot of 3D parameter subspace formed by a selected tissue property for the three tissues liver, tumor, and vessel. The distribution of parameter settings of the simulation ensemble is shown in grey, while the currently selected parameter setting is highlighted in green and its k-nearest neighbors in blue.

3.5. Deep Learning Prediction

For a parameter-space analysis that allows for continuously changing the parameter values (Task T5), one would theoretically need access to simulation runs for each parameter setting. As running simulations are computationally expensive, this is far from being possible within an interactive setting. Hence, one would need a means to efficiently predict the simulation outcome. In our original paper [HEG*22], we proposed to use scattered data interpolation of the simulation output applied to the k nearest neighbors in parameter space (cf. Figure 3), which requires a densely sampled parameter space for good "predictions". Here, we propose to use a *deep learning* approach for improved predictions. Moreover, the parameter-space interpolation [HEG*22] assumes that the spatial configurations, i.e., size and location of the tissues involved as well as the needle position, remain static. With our deep learning approach, we facilitate predictions for new spatial configurations, in particular, for testing different needle positions.

Prediction Goal and Data Generation. The outcome of an RF ablation simulation is a 3D temperature field. Thus, our aim is to predict the temperature field, i.e., the *output layer* of our deep learning approach should be a 3D temperature field. The input to the RF ablation simulation is a segmentation of the respective volume into the tissues involved and the parameters that describe the tissue properties. The segmentation labels each voxel as tumor, blood vessel, liver, needle, or other tissue (where "other tissue" is not used during simulation). Figure 4 shows a slice view of the segmentation volume. To generate the input of our deep learning approach, we assign to each voxel the tissue properties based on the tissue label. A distinguishable value (-1) is assigned to needle's voxels ("other tissue" gets assigned zero values). As our prior analysis results [HEG*22] revealed that the relative blood perfusion rate is the main tissue property that influences the simulation outcome, we will focus on the relative blood perfusion rate in the following.

Assigning the tissue parameters to the respective voxels allows us to capture not only the parameter values for the tissue types but also combine them with the spatial locations of the tissue. Thus, the *input layer* of our deep learning approach is a single, piecewise constant 3D scalar field. In our implementation, the scalar field consists $92 \times 92 \times 92$ voxels, which defines the size of the input layer.

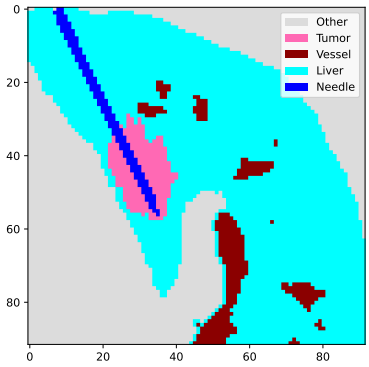

Figure 4: Slice view of the segmentation volume. For the input of the deep neural network, we store the parameter values of the respective tissue properties for each voxel ("other tissue" gets assigned value 0, "needle" value -1).

Network Architecture Design. Since the input and output layers are both 3D fields, we employ a 3D *Convolutional Neural Network* (CNN) to capture spatial coherence and local heat-diffusion patterns of temperature fields while maitaining fast inference for interactive use within TPAT. CNNs have achieved great success in the deep learning field for extracting features from data with convolution structures [LLY*22, KSZQ20]. Figure 5 shows an overview of the architecture of our CNN model. The input layer represents a single 3D scalar field and, thus, in our implementation is of size $92 \times 92 \times 92 \times 1$. The following layers make use of a convolution–pooling sequence, inspired by famous networks like AlexNet [KSH17], VGG-16, VGG-19 [SZ15a, SZ15b, SZ15c], and ResNet [HZRS16]. We use the most popular convolutional kernel for 3D images of size $3 \times 3 \times 3$. The size of the layers is halved after each max-pooling layer for each spatial dimension, while the number of channels is increased. To reach the desired output shape of $92 \times 92 \times 92 \times 1$ (size of the temperature field), the convolution and pooling layers are followed by a flattening operation, two dense layers, and a reshaping step. The network consists of a sequence of 3D convolution and pooling layers, which progressively extract spatial features and reduce the resolution in a controlled manner. Convolution layers capture localized temperature patterns and spatial gradients relevant to heat propagation, while pooling increases the receptive field and enables the model to integrate information across larger tissue regions. After the convolution–pooling sequence, the feature maps are flattened, allowing the subsequent fully connected layers to combine global spatial information for the final prediction of the temperature field. These standard operations are widely used in volumetric prediction tasks and were chosen for their robustness and interpretability [LLY*22, KSH17, SZ15a, SZ15b, SZ15c].

For the training process, we use standard settings: We apply the ReLU (rectified linear unit) function as the activation function of

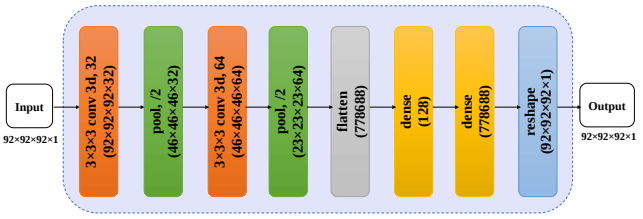

Figure 5: CNN architecture, where layers are color-coded by their type and the shape of each layer is provided. Our model consists of two convolutional layers, each of which is followed by a max-pooling layer. Further layers transform to the desired shape of the output layer.

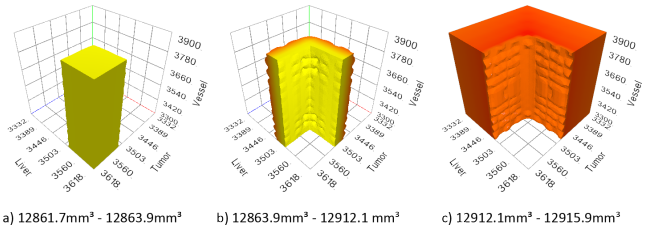

Figure 6: Ablation data plot of ablation volume with respect to heat capacity: The three surfaces exhibit a similar impact of the liver's and tumor's heat capacity on the ablation volume, while the vessels' heat capacity has no influence.

the convolutional layers, apply the Adam optimizer (a stochastic gradient approach with adaptive learning rate), and use the mean-squared error (MSE) as loss function. To avoid overfitting, we stop the training process according to the early-stopping policy, i.e., if there is no further decrease in loss for a specified number of epochs (patience=50).

4. Analysis of Tissue Properties

We apply TPAT to analyze the effect of the tissue properties on RF ablation. We generate multiple simulation ensembles with 96 to 225 simulation runs per ensemble to investigate 10 different tissue properties (changing one or multiple properties within an ensemble) as well as different spatial arrangements (changing tumor size and/or location) [HEG*22]. In the following, we report the main findings when modifying a single tissue property (i.e., when changing the three parameters of this property for the three tissues involved) to generate ensembles.

To get a first impression of the simulation outcomes, we start by investigating the ablation areas of an ensemble member with average tissue properties in a 3D spatial visualization, see Figure 1a. We observe that most of the tumor (pink) is located inside the ablation area (green), but some parts of the tumor are not ablated and, on the other hand, parts outside the tumor get ablated. We also observe that vessel structures (red) are rather close to the ablation area and, thus, influence the ablation process.

Then, we analyze the individual tissue properties one by one. We start by varying the *density* of the three different tissues, i.e., we change the three parameters density of liver, density of tumor, and density of vessel. When doing so, the ablation volume varies between 12 843.3 mm^3 and 12 923.1 mm^3 resulting in a difference of 79.8 mm^3, which is a change of only 0.62% when relating the difference to the average ablation volume. When only considering the tumor, its ablated volume difference is 2.95 mm^3 or 0.066%. Hence, we can conclude that density is an almost negligible property.

When investigating the impact of *heat capacity*, we observe that its effect is even smaller with a change in ablation area of 0.42% and in ablated tumor of 0.04%. When visualizing the 3D parameter space in the ablation data plot in Figure 6, we observe that the heat capacity of the liver and tumor have approximately equal impact on the ablation volume size, while the heat capacity of the vessel does not impact the simulation output at all.

When performing a similar analysis on the *thermal conductivity*, we observe that this property has a higher impact with an ablation volume difference of 2.676%. Here, the liver's thermal conductivity has the highest influence on the ablation volume with a difference of 2.694 $\mathrm{m}^3/(10^{-3}\mathrm{W/mK})$, followed by the one for tumor, which is still on a similar scale. However, while an increasing liver's thermal conductivity decreases the ablation volume, an increasing tumor's thermal conductivity increases the ablation volume. The vessel's thermal conductivity only has an almost negligible effect.

As a fourth parameter, we investigate the influence of *relative blood perfusion rate*, which has by far the most influence on the ablation volume (difference of 103.7%) and the tumor ablation volume (difference of 7.4%). The vessel's relative blood perfusion rate is not used by the simulation tool and thus has no impact. We observe that the liver has a much higher effect on the ablation volume (difference of 77.329 $\mathrm{m}^3/(10^{-4}\mathrm{ml}/(\mathrm{s}\cdot\mathrm{cm}))$) than the tumor (difference of 17.761 $\mathrm{m}^3/(10^{-4}\mathrm{ml}/(\mathrm{s}\cdot\mathrm{cm}))$), while they both have a similar impact on the tumor ablation volume. We conclude that a reduced liver's relative blood perfusion rate results in a larger ablation of healthy tissue.

Since relative blood perfusion rate is the most influential parameter, we further investigate its influence on ablation volume and tumor ablation volume using the ablation data plots shown in Figures 7 and 8, respectively. We generate four surfaces for equally sized ablation volume intervals in Figure 7. The surfaces indicate that an increase in the relative blood perfusion rate results in a reduced impact on the ablation volume size, as the coverage of the parameter space gets smaller for intervals of higher values. Thus, when the values are smaller, a one-unit increase in the blood perfusion rate has a stronger impact on the ablation volume. When performing an analogous investigation of the tumor ablation volume in Figure 8, we observe, however, that the influence of both relative blood perfusion rates on the tumor ablation increases as the parameter values increase. We conclude that, in both cases, a non-linear change can be observed when the parameter range is linearly changed, as evidenced by the different sizes of the regions when the parameter interval sizes remain constant.

While the global impact of parameters on the simulation is of high importance, it is similarly important to investigate, which spatial regions are affected most by the parameter changes. Figure 9

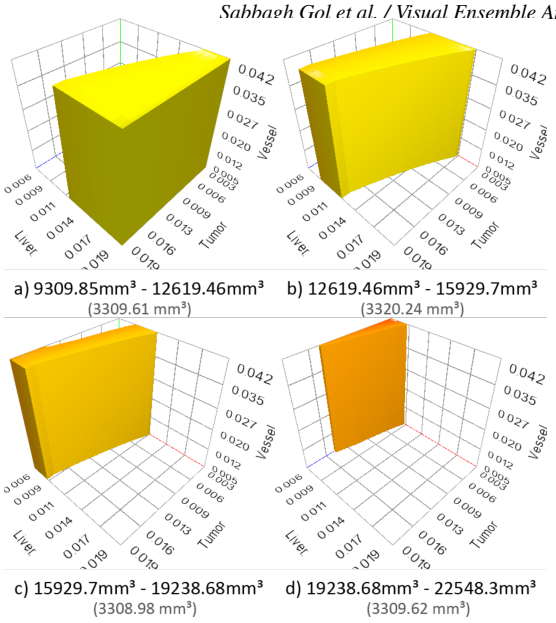

Figure 7: Ablation data plot of ablation volume for relative blood perfusion rate: The four surfaces of evenly sized ablation volume intervals indicate that, as the relative blood perfusion rates of liver increases, the impact on the tumor ablation volume decreases non-linearly.

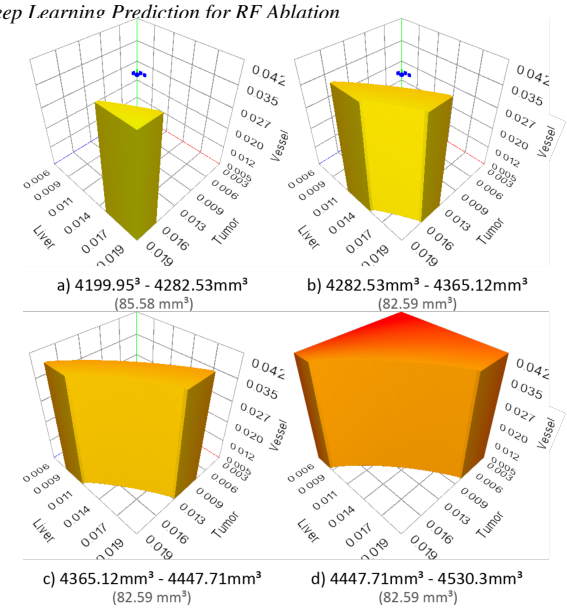

Figure 8: Ablation data plot of ablation tumor volume for relative blood perfusion rate: The four surfaces of evenly sized ablation tumor volume intervals indicate that, as the relative blood perfusion rates of both liver and tumor increase, the impact on the tumor ablation volume increases non-linearly.

shows juxtaposed 2D and 3D spatial visualizations that illustrate the effects of low and high relative blood perfusion rates of the liver and tumor tissues on the ablation outcome in different spatial regions. While the relative blood perfusion rate of the tumor mostly affects the area surrounding the tumor, the liver's relative blood perfusion rate leads to a more uniform expansion or reduction of the entire ablation volume. As the figures also indicate a strong impact of the vessels on the ablation volume, we further inspect the role of the relative blood perfusion rate close to a vessel in Figure 10. The comparative 3D spatial visualizations show that the impact of the relative blood perfusion rate significantly decreases in the vicinity of blood vessels.

We also analyzed the remaining six tissue properties, but none of them exhibited any impact on the simulation outcome. We shared our tool with our domain experts from the field of RF ablation simulation, have them analyze the ensemble data, and obtained their *feedback* on the tool and the findings. The tool allowed them to confirm their hypotheses about the different influences of the various tissue properties. They also confirmed that some tissue properties have negligible influence on the outcome of the simulation model. They particularly appreciated the spatial visualizations, because they clearly showed the impact of the position of the vessels on the safety margins around the tumor. In contrast to tabulated numerical values, our approach allows them to visually investigate the spatial variations. They were also interested in investigating the nonlinearity of the dependencies. The ablation data plots showed them that a linear change in the tissue properties might lead to nonlinear variations in the ablation quantities, such as the volume of ablation.

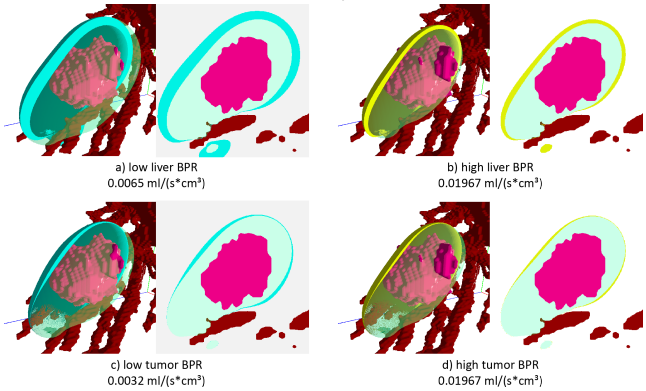

Figure 9: 2D and 3D spatial visualizations allow for the comparison of the ablation volume when changing the blood perfusion rate. The 3D volumes have been clipped to better observe the thickness of the ablation volume expansion (cyan) and reduction (yellow). The liver's relative blood perfusion leads to a more uniform expansion or reduction of the entire volume (top), while the tumor's relative blood perfusion rate of the tumor primarily affects the area surrounding the tumor (button). In both cases, the cooling effect of vessels can be observed, indicating their strong impact on the ablation process.

The main criticism of the domain scientists for the first version of TPAT [HEG*22] was the creation of large ensembles to perform the analyses. Handling such large amounts of data is challenging and the analysis can be time-consuming due to loading times for the data. This main criticism led to the extension of our work, where we now use deep learning predictions of simulation results presented in Section 3.5, which allows us to work with much smaller ensem-

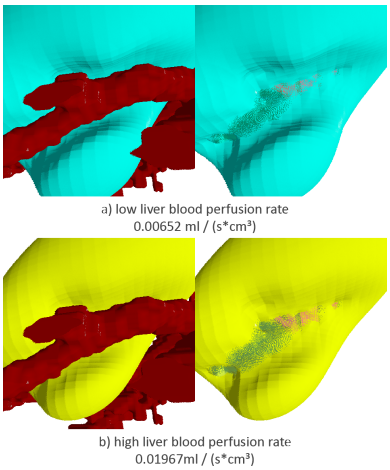

Figure 10: Comparative volume visualizations of runs with low and high relative blood perfusion rates for liver exhibit that there is no influence close to blood vessels.

bles while still fulfilling Task T5 on continuous parameter-space analysis. In the next section, we evaluate this extension.

5. Simulation Results for Deep Learning Prediction

To generate training and test data for our deep learning approach, we randomly sampled the 3D parameter space spanned by the relative blood perfusion rate for liver, tumor, and vessels (cf. Figure 3). In addition, we sampled different spatial configurations, where we performed translations to the tumor by 0, 2, 4, 6, 8, or 10 voxels in z-direction and/or by 0 or 10 voxels in negative y-direction as well as a shrinkage or expansion of tumor (up to 3 voxels) and/or vessels (up to 1 voxel). We selected 36 among those spatial configurations, cf. [HEG*22]. We randomly sample, which requires less samples when compared to uniform sampling but still covers all parameters. In addition, we randomly translated the needle position within the tumor by up to 2 voxels in positive or negative x- and/or y-direction, leading to 25 different needle positions within the tumor. For each of the 36 spatial configurations, we ran 150 simulation runs (with different tissue parameter settings and needle positions), leading to 5,400 simulation runs in total. One spatial configuration was excluded from the training data and, for the remaining 35 spatial configurations, we selected 80% of the data (i.e., 4,200 simulation runs) for training the deep neural network. The excluded spatial configuration as well as the remaining 20% of the data from the other 35 spatial configurations were used for testing. We will next present the prediction results for these two test cases.

Prediction Within Spatial Configurations. In our first experiment, we predict the simulation outcome for the test data (1,050 simulation runs) from the 35 spatial configurations that were used for training. We compare the deep learning predictions to the interpolation results obtained by scattered data interpolation using an inverse-distance-based approach [She68] computed from k nearest neighbors as performed in our previous work [HEG*22]. Note that for the interpolation, we only used those simulation runs that had the same spatial configuration, while our deep neural network was trained on all 35 spatial configurations simultaneously.

To compare the deep learning prediction and scattered data interpolation results, we calculate the difference between prediction and interpolation results from the simulation ground truth in terms of ablation volume size, ablation volume of healthy tissues, and ablation volume of tumor, as these measures were considered most relevant by the domain experts. These quantities were identified as the most relevant by collaborating domain experts, as they directly reflect treatment efficacy and safety, and provide a clinically meaningful validation of the deep learning predictions. The deviations are computed by the amount of different voxels multiplied by the volumetric voxel size. Figure 11 shows the boxplots of the deviations when considering all 1,050 simulation runs. We observe that the deviations are lower for the deep learning prediction for all three measures. To compare the prediction and interpolation results, a statistical significance test (Wilcoxon Signed-Rank Test) is calculated. The p-values provided on top of Figure 11 are extremely small, i.e., far below any common significance level (e.g., 0.05, 0.01, or even 0.001), we can strongly reject the null hypothesis, i.e., there is a statistically significant difference between the deep learning predictions and the interpolation results. Since the boxplots show aggregated data, one cannot relate individual results to each other. Therefore, we also provide a scatterplot in Figure 12. It demonstrates that for the 94.32% of the test data the deep learning prediction is better than interpolation.

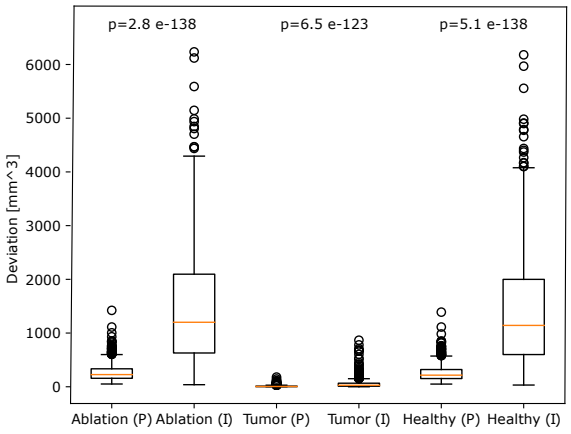

Figure 11: Deviation of deep learning prediction from ground truth (labeled with P) compared to the deviation of the interpolation result from ground truth (labeled with I) for ablation, ablated tumor, and ablated healthy volume for novel parameter settings of known spatial configurations. The improvements using deep learning is strongly statistically significant.

For a better understanding of the results, we visually investigate the test sample with the worst interpolation quality. The interpolation result of this sample has the highest deviation from its ground truth. Slices of this result are shown in Figure 13. It shows a slice view of slice 45 that for this test data, the ablation volume that resulted from the interpolation method lacks a significant number of voxels in comparison to our CNN model prediction. The supplementary material provides a detailed quantitative evaluation

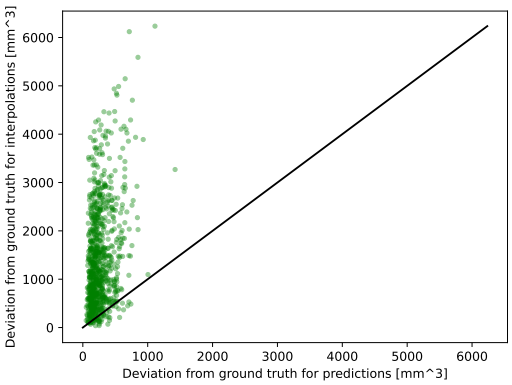

Figure 12: Comparison of deviations of ablated volume from ground truth shows a better performance of deep learning prediction over interpolation results in 94.32% of all cases.

of CNN prediction versus interpolation-based schemes, including voxel-count deviations, RMSE, IoU, and Dice coefficients for all test cases within spatial configurations.

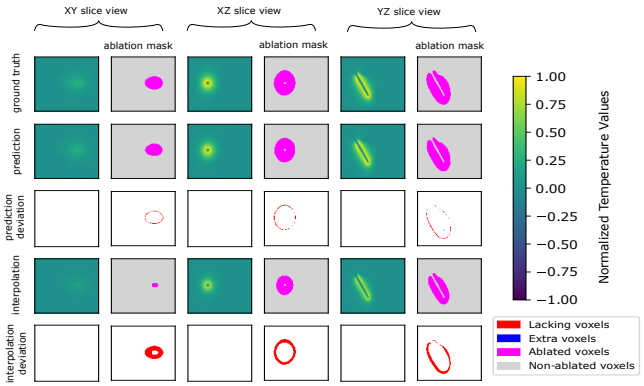

Figure 13: Comparison of ground truth, deep learning prediction, and scattered data interpolation for novel parameter settings of known spatial configurations. The first, second, and fourth rows show ground truth, prediction, and interpolation outcomes, where the ablation mask is illustrated with pink color. The third and fifth rows show the difference of prediction and interpolation results from ground truth, where red color is an indicator of lacking voxels while blue color shows extra voxels from the ground truth.

Prediction Across Spatial Configurations. In the second experiment, we evaluate how well a novel spatial configuration can be predicted. The spatial configuration that had been excluded from training was the one, where the tumor was translated by six voxels in z-direction (no other modifications). The test data consists of 150 simulation runs for this spatial configuration. To compare our deep learning approach to interpolation, we have to extend the interpolation approach. To obtain the interpolation result, we first perform scattered data interpolations within the spatial configurations, where the tumor had been translated by four or eight voxels, respectively, and then linearly interpolate between those intermediate interpolation results.

Figure 14 shows the boxplots of ablated volume deviations analogously to Figure 11. Again, we observe that the deviations of all three computed volumes are significantly smaller for the deep learning predictions when compared to the interpolation results. The p-values are, again, computed using Wilcoxon Signed-Rank Test. We also provide a scatterplot that exhibits the deviations for each prediction-interpolation pair in Figure 15. It shows that in 99.07% of all test cases the deep learning prediction is better.

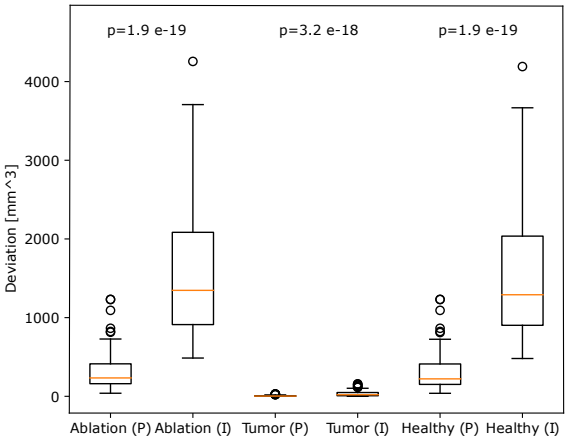

Figure 14: Deviation of deep learning prediction from ground truth (labeled with P) compared to the deviation of the interpolation result from ground truth (labeled with I) for ablation, ablated tumor, and ablated healthy volume for a new spatial configuration. The improvements using deep learning is strongly statistically significant.

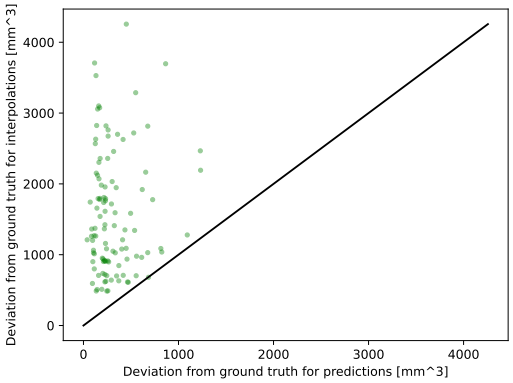

Figure 15: Comparison of deviations of ablated volume from ground truth shows a better performance of deep learning prediction over interpolation results in 99.07% of all cases.

We also provide a visual comparison of the worst interpolation result to the deep learning prediction and ground truth in Figure 16. We observe that the interpolation underestimates the extent of the ablated area and that the position of the needle is not well represented. This behavior was expected as the interpolation is performed linearly per voxel and, thus, the interpolated value needs to be between the two temperature values used for the linear interpolation. These results show that the deep learning approach does not only produce better results for existing spatial configurations but

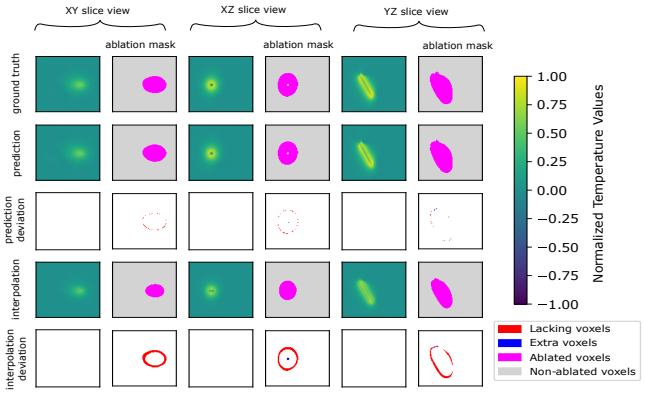

Figure 16: Comparison of ground truth, deep learning prediction, and scattered data interpolation for novel spatial configuration. The first, second, and fourth rows show ground truth, prediction, and interpolation outcomes, where the ablation mask is illustrated with pink color. The third and fifth rows show the difference of prediction and interpolation results from ground truth, where red color is an indicator of lacking voxels while blue color shows extra voxels from the ground truth.

also supports the fast prediction of temperature fields for previously unseen configurations. See supplementary material for a detailed quantitative evaluation of CNN prediction versus interpolation-based schemes, including voxel-count deviations, RMSE, IoU, and Dice coefficients for all test cases across spatial configurations.

6. Discussion and Conclusion

This paper discusses the effect of tissue properties on RF ablation using the Tissue Property Analysis Tool (TPAT), which is supported by a CNN to predict new simulation results. The integration of deep learning within TPAT improves the accuracy of predicted results and enables more comprehensive analyses. Spatial visualizations are created to compare different tissue properties and analyze their influence on the ablation outcome. Parameter space visualizations help to analyze the whole ensemble. The tool enables a more thorough examination of how tissue properties affect clinical treatments, aiding in the identification of the most critical properties and the regions where their influence is most significant. As a result, clinicians can determine which important factors should be incorporated into treatment plans, and the margins around the tumor could incorporate this information. The prediction of RF ablation outcome according to new parameter settings using a deep learning network allows for a smooth exploration in parameter space. Even though our approach focuses on RF ablation, it can be easily utilized for other treatment methods to detect and analyze significant parameters in corresponding simulations. Our tool is capable of handling a range of ensemble sizes effectively. The ablation data plot also scales well with the number of tissue properties.

The tool was developed in close collaboration with domain experts throughout all design phases. The expert group consisted of two researchers specializing in RF ablation simulation and computational modeling. Their involvement evolved from early task definition and data interpretation to iterative feedback on visualization prototypes and model outputs. Key takeaways include the importance of interpretable, clearly recognized quantitative measures and real-time responsiveness for exploring unseen parameter settings, which guided both the visualization design and the integration of the deep learning surrogate. This feedback directly motivated the integration of the deep learning surrogate, enabling real-time prediction of simulation outcomes and continuous parameter exploration without extensive data loading. In addition, experts expressed a preference for spatial representations over purely tabulated summaries, reinforcing our focus on spatial visual encodings. In discussion with domain experts, TPAT was found to be a useful tool to ensure that the safety margins around tumors would enclose the target for a reasonable range of material properties. It was stated that the material properties are heterogeneous, i.e., tissue types were averaged values drawn from a distribution, and that perhaps metrics, such as the averaged ablated volumes, could be computed based on a mean and standard deviation, rather than a single value. Because obtaining accurate material parameters is beyond the practical scope of this work, the use of a machine-learning surrogate is well-suited for exploring a wide range of possible parameter settings. To assess the integration of the deep learning surrogate, they explored ablation outcomes under varying tissue parameter configurations. Experts reported that the surrogate maintained expected trends and did not introduce implausible spatial artifacts.

Visualization researchers benefit from this work as an example of how predictive models can be incorporated into interactive visual analysis tools to enable dense sampling of multi-dimensional parameter spaces without computationally expensive ensemble generation. The main contributions for the visualization community are: (1) A workflow for continuous parameter-space exploration that combines predicted fields with established spatial visualization techniques. (2) A demonstration of how ML-based surrogate models can enhance, rather than replace, visual analysis.

Further research could focus on visualizing ablation metrics for more than three tissue types and including segmentation uncertainty. This would also increase its relevance to other medical applications. A structured user evaluation involving additional researchers not involved in the tool's development would also be beneficial for the approach's continued development. As the surrogate model produces deterministic predictions, the current implementation does not provide explicit uncertainty estimates. Quantitative evaluation on 1,050 simulation runs shows that the surrogate model achieves a mean relative ablation volume error of 3.13% (±1.80%), in 95% of the cases below 6.57%, indicating bounded approximation uncertainty that remains small relative to clinically relevant safety margin assessments. A limitation of this work is that the surrogate was trained on variations of a single patient anatomy with varied tissue properties and spatial configurations. Broader generalization to substantially different anatomies would require additional patient data and retraining.

Acknowledgments

This work was funded by the Deutsche Forschungsgemeinschaft (DFG, German Research Foundation) grants 241370238 (LI 1530/19-2, PR 1038/6-2) and 260446826 (LI 1530/21-2).

References

[ALHG08] AHMED M., LIU Z., HUMPHRIES S., GOLDBERG S. N.: Computer modeling of the combined effects of perfusion, electrical conductivity, and thermal conductivity on tissue heating patterns in radiofrequency tumor ablation. *International Journal of Hyperthermia 24*, 7 (2008), 577–588. doi:10.1080/02656730802192661.

[Ber06] BERJANO E.: Theoretical modeling for radiofrequency ablation: State-of-the-art and challenges for the future. *Biomedical Engineering Online 5* (2006), 24. doi:10.1186/1475-925X-5-24.

[BFAC18] BARAJAS M., FRAGA T., ACEVEDO M., CABRERA R. G.: Radiofrequency ablation: a review of current knowledge, therapeutic perspectives, complications, and contraindications. *International Journal of Biosensors & Bioelectronics 4* (2018), 53–55. doi:10.15406/ijbsbe.2018.04.00098.

[BKM*06] BRICAULT I., KIKINIS R., MORRISON P. R., VANSONNENBERG E., TUNCALI K., SILVERMAN S. G.: Liver metastases: 3D shape-based analysis of CT scans for detection of local recurrence after radiofrequency ablation. *Radiology 241*, 1 (2006), 243–250. doi:10.1148/radiol.2411050987.

[BM10] BRUCKNER S., MÖLLER T.: Result-driven exploration of simulation parameter spaces for visual effects design. *IEEE Transactions on Visualization and Computer Graphics 16*, 6 (2010), 1468–1476. doi:10.1109/tvcg.2010.190.

[BPM*15] BOCK A., PEMBROKE A., MAYS M. L., RASTAETTER L., ROPINSKI T., YNNERMAN A.: Visual verification of space weather ensemble simulations. In *2015 IEEE Scientific Visualization Conference (SciVis)* (2015), IEEE, pp. 17–24. doi:10.1109/SciVis.2015.7429487.

[CWB*19] CHEN C., WANG C., BAI X., ZHANG P., LI C.: Generativemap: Visualization and exploration of dynamic density maps via generative learning model. *IEEE Transactions on Visualization and Computer Graphics 26*, 1 (2019), 216–226. doi:10.1109/TVCG.2019.2934806.

[CZW*19] CUI W., ZHANG X., WANG Y., HUANG H., CHEN B., FANG L., ZHANG H., LOU J.-G., ZHANG D.: Text-to-viz: Automatic generation of infographics from proportion-related natural language statements. *IEEE Transactions on Visualization and Computer Graphics 26*, 1 (2019), 906–916. doi:10.1109/TVCG.2019.2934785.

[DD19] DIBIA V., DEMIRALP Ç.: Data2vis: Automatic generation of data visualizations using sequence-to-sequence recurrent neural networks. *IEEE Computer Graphics and Applications 39*, 5 (2019), 33–46. doi:10.1109/MCG.2019.2924636.

[EL22] EVERS M., LINSEN L.: Multi-dimensional parameter-space partitioning of spatio-temporal simulation ensembles. *Computers & Graphics 104* (2022), 140–151. doi:10.1016/j.cag.2022.04.005.

[ELRL24] EVERS M., LEISTIKOW S., RAVE H., LINSEN L.: Interactive visual analysis of spatial sensitivities. *IEEE Transactions on Visualization and Computer Graphics* (2024). doi:10.1109/TVCG.2024.3433001.

[FKRW17] FERSTL F., KANZLER M., RAUTENHAUS M., WESTERMANN R.: Time-hierarchical clustering and visualization of weather forecast ensembles. *IEEE Transactions on Visualization and Computer Graphics 23*, 1 (2017), 831–840. doi:10.1109/tvcg.2016.2598868.

[HEG*22] HEIMES K., EVERS M., GERRITS T., GYAWALI S., SINDEN D., PREUSSER T., LINSEN L.: Studying the effect of tissue properties on radiofrequency ablation by visual simulation ensemble analysis. In *Eurographics Workshop on Visual Computing for Biology and Medicine* (2022), Raidou R. G., Sommer B., Kuhlen T. W., Krone M., Schultz T., Wu H.-Y., (Eds.), The Eurographics Association. doi:10.2312/vcbm.20221187.

[HHB16] HAO L., HEALEY C. G., BASS S. A.: Effective visualization of temporal ensembles. *IEEE Transactions on Visualization and Computer Graphics 22*, 1 (2016), 787–796. doi:10.1109/tvcg.2015.2468093.

[HL22] HUESMANN K., LINSEN L.: SimilarityNet: A deep neural network for similarity analysis within spatio-temporal ensembles. *Computer Graphics Forum* (2022). doi:10.1111/cgf.14548.

[HWG*19] HE W., WANG J., GUO H., WANG K.-C., SHEN H.-W., RAJ M., NASHED Y. S., PETERKA T.: InSituNet: Deep image synthesis for parameter space exploration of ensemble simulations. *IEEE Transactions on Visualization and Computer Graphics 26*, 1 (2019), 23–33.

[HZRS16] HE K., ZHANG X., REN S., SUN J.: Deep residual learning for image recognition. In *Proceedings of the IEEE Conference on Computer Vision and Pattern Recognition* (2016), pp. 770–778. doi:10.1109/CVPR.2016.90.

[KBL19a] KAPPE C., BÖTTINGER M., LEITTE H.: Analysis of decadal climate predictions with user-guided hierarchical ensemble clustering. *Computer Graphics Forum 38*, 3 (2019), 505–515. doi:10.1111/cgf.13706.

[KBL19b] KAPPE C. P., BOTTINGER M., LEITTE H.: Exploring variability within ensembles of decadal climate predictions. *IEEE Transactions on Visualization and Computer Graphics 25*, 3 (2019), 1499–1512. doi:10.1109/tvcg.2018.2810919.

[KSH17] KRIZHEVSKY A., SUTSKEVER I., HINTON G. E.: ImageNet classification with deep convolutional neural networks. *Communications of the ACM 60*, 6 (2017), 84–90. doi:10.1145/3065386.

[KSZQ20] KHAN A., SOHAIL A., ZAHOORA U., QURESHI A. S.: A survey of the recent architectures of deep convolutional neural networks. *Artificial Intelligence Review 53* (2020), 5455–5516.

[LLY*22] LI Z., LIU F., YANG W., PENG S., ZHOU J.: A survey of convolutional neural networks: Analysis, applications, and prospects. *IEEE Transactions on Neural Networks and Learning Systems 33*, 12 (2022), 6999–7019. doi:10.1109/TNNLS.2021.3084827.

[LQT*18] LUO Y., QIN X., TANG N., LI G., WANG X.: Deepeye: Creating good data visualizations by keyword search. In *Proceedings of the 2018 International Conference on Management of Data* (2018), Das G., Jermaine C. M., Bernstein P. A., (Eds.), pp. 1733–1736. doi:10.1145/3183713.3193545.

[ME19] MA B., ENTEZARI A.: An interactive framework for visualization of weather forecast ensembles. *IEEE Transactions on Visualization and Computer Graphics 25*, 1 (2019), 1091–1101. doi:10.1109/tvcg.2018.2864815.

[OBJ15] OBERMAIER H., BENSEMA K., JOY K. I.: Visual trends analysis in time-varying ensembles. *IEEE Transactions on Visualization and Computer Graphics 22*, 10 (2015), 2331–2342. doi:10.1109/tvcg.2015.2507592.

[OKB*19] ORBAN D., KEEFE D. F., BISWAS A., AHRENS J., ROGERS D.: Drag and track: A direct manipulation interface for contextualizing data instances within a continuous parameter space. *IEEE Transactions on Visualization and Computer Graphics 25*, 1 (2019), 256–266. doi:10.1109/tvcg.2018.2865051.

[PBCR11] PRETORIUS A. J., BRAY M.-A., CARPENTER A. E., RUDDLE R. A.: Visualization of parameter space for image analysis. *IEEE Transactions on Visualization and Computer Graphics 17*, 12 (2011), 2402–2411. doi:10.1109/tvcg.2011.253.

[PPA*12] PHADKE M. N., PINTO L., ALABI O., HARTER J., TAYLOR II R. M., WU X., PETERSEN H., BASS S. A., HEALEY C. G.: Exploring ensemble visualization. In *Visualization and Data Analysis 2012* (2012), Wong P. C., Kao D. L., Hao M. C., Chen C., Kosara R., Livingston M. A., Park J., Roberts I., (Eds.), vol. 8294, International Society for Optics and Photonics, p. 82940B. doi:10.1117/12.912419.

[PWB*09] POTTER K., WILSON A., BREMER P.-T., WILLIAMS D., DOUTRIAUX C., PASCUCCI V., JOHNSON C. R.: Ensemble-Vis: A framework for the statistical visualization of ensemble data. In *2009 IEEE International Conference on Data Mining Workshops* (2009), IEEE, pp. 233–240. doi:10.1109/ICDMW.2009.55.

[RCMM*16] RAIDOU R., CASARES-MAGAZ O., MUREN L., VAN DER

HEIDE U., RØRVIK J., BREEUWER M., VILANOVA A.: Visual analysis of tumor control models for prediction of radiotherapy response. *Computer Graphics Forum 35*, 3 (2016), 231–240. doi:10.1111/cgf.12899.

[RGH*19] RISTOVSKI G., GARBERS N., HAHN H., PREUSSER T., LINSEN L.: Uncertainty-aware visual analysis of radiofrequency ablation simulations. *Computers & Graphics 79* (2019), 24–35. doi:10.1016/j.cag.2018.12.005.

[RWS*10] RIEDER C., WEIHUSEN A., SCHUMANN C., ZIDOWITZ S., PEITGEN H.-O.: Visual support for interactive post-interventional assessment of radiofrequency ablation therapy. *Computer Graphics Forum 29*, 3 (2010), 1093–1102. doi:10.1111/j.1467-8659.2009.01665.x.

[SCTL05] SHEU T. W. H., CHOU C. W., TSAI S. F., LIANG P. C.: Three-dimensional analysis for radio-frequency ablation of liver tumor with blood perfusion effect. *Computer Methods in Biomechanics and Biomedical Engineering 8*, 4 (2005), 229–40. doi:10.1080/10255840500289731.

[SHB*14] SEDLMAIR M., HEINZL C., BRUCKNER S., PIRINGER H., MÖLLER T.: Visual parameter space analysis: A conceptual framework. *IEEE Transactions on Visualization and Computer Graphics 20*, 12 (2014), 2161–2170. doi:10.1109/tvcg.2014.2346321.

[She68] SHEPARD D.: A two-dimensional interpolation function for irregularly-spaced data. In *Proceedings of the 1968 23rd ACM National Conference* (New York, NY, USA, 1968), Blue R. B., Rosenberg A. M., (Eds.), ACM '68, ACM, pp. 517–524. doi:10.1145/800186.810616.

[STDS95] SPENCE B., TWEEDIE L., DAWKES H., SU H.: Visualization for functional design. In *Proceedings of the 1995 IEEE Symposium on Information Visualization* (Washington, DC, USA, 1995), Gershon N. D., Eick S. G., (Eds.), INFOVIS '95, IEEE Computer Society, pp. 4–10. doi:10.1109/infvis.1995.528680.

[SWS19] SMART S., WU K., SZAFIR D. A.: Color crafting: Automating the construction of designer quality color ramps. *IEEE Transactions on Visualization and Computer Graphics 26*, 1 (2019), 1215–1225. doi:10.1109/TVCG.2019.2934284.

[SXL*22] SHI N., XU J., LI H., GUO H., WOODRING J., SHEN H.-W.: VDL-Surrogate: A view-dependent latent-based model for parameter space exploration of ensemble simulations. *IEEE Transactions on Visualization and Computer Graphics 29*, 1 (2022), 820–830. doi:10.1109/TVCG.2022.3209413.

[SZ15a] SIMONYAN K., ZISSERMAN A.: Very deep convolutional networks for large-scale image recognition. In *3rd International Conference on Learning Representations (ICLR 2015)* (2015), Computational and Biological Learning Society, pp. 1–14. doi:https://arxiv.org/abs/1409.1556v6.

[SZ15b] SIMONYAN K., ZISSERMAN A.: Very deep convolutional networks for large-scale image recognition, 2015. arXiv:1409.1556.

[SZ15c] SIMONYAN K., ZISSERMAN A.: Very deep convolutional networks for large-scale image recognition. *arXiv preprint arXiv:1409.1556* (2015). doi:10.48550/arXiv.1409.1556.

[SZD*10] SANYAL J., ZHANG S., DYER J., MERCER A., AMBURN P., MOORHEAD R.: Noodles: A tool for visualization of numerical weather model ensemble uncertainty. *IEEE Transactions on Visualization and Computer Graphics 16*, 6 (2010), 1421–1430. doi:10.1109/TVCG.2010.181.

[WH23] WANG C., HAN J.: DL4SciVis: A state-of-the-art survey on deep learning for scientific visualization. *IEEE Transactions on Visualization and Computer Graphics 29*, 8 (2023), 3714–3733. doi:10.1109/TVCG.2022.3167896.

[WHLS19] WANG J., HAZARIKA S., LI C., SHEN H.-W.: Visualization and visual analysis of ensemble data: A survey. *IEEE Transactions on Visualization and Computer Graphics 25*, 9 (2019), 2853–2872. doi:10.1109/tvcg.2018.2853721.

[WJW*19] WANG Y., JIN Z., WANG Q., CUI W., MA T., QU H.: Deepdrawing: A deep learning approach to graph drawing. *IEEE Transactions on Visualization and Computer Graphics 26*, 1 (2019), 676–686. doi:10.1109/TVCG.2019.2934798.

[WLSL17] WANG J., LIU X., SHEN H.-W., LIN G.: Multi-resolution climate ensemble parameter analysis with nested parallel coordinates plots. *IEEE Transactions on Visualization and Computer Graphics 23*, 1 (2017), 81–90. doi:10.1109/tvcg.2016.2598830.

[ZHXS25] ZHAO Z., HU Y., XU L. X., SUN J.: Advancements in deep learning for image-guided tumor ablation therapies: a comprehensive review. *Progress in Biomedical Engineering* (2025).